machines

MDPI

Article

Simulation and Analysis of Electric Thermal Coupling for Corrosion Damage of Metro Traction Motor Bearings

Haisheng Yang [1], Zhanwang Shi [1], Xuelan Wang [2], Jiahang Zhang [1], Run Zhang [1] and Hengdi Wang [1,*]

[1] School of Mechatronics Engineering, Henan University of Science and Technology, Luoyang 471003, China; yhs@haust.edu.cn (H.Y.); 230320010057@stu.haust.edu.cn (Z.S.); 230320010023@stu.haust.edu.cn (J.Z.); 230320010110@stu.haust.edu.cn (R.Z.)
[2] Ningbo Great Group Co., Ltd., Yuyao 315482, China; wangxl@ngtb.cn
* Correspondence: 9901432@haust.edu.cn; Tel.: +86-0379-64231479

Abstract

With the electrification of generator sets, electric locomotives, new energy vehicles, and other industries, AC motors subject bearings to an electric field environment, leading to galvanic corrosion due to the use of variable frequency power supply drives. The phenomenon of bearing discharge breakdown in subway traction motors is a critical issue in understanding the relationship between shaft current strength and the extent of bearing damage. This paper analyzes the mechanism of impulse discharge that leads to galvanic corrosion damage in bearings at a microscopic level and conducts electric thermal coupling simulations of the traction motor bearing discharge breakdown process. It examines the temperature rise associated with lubricant film discharge breakdown during the dynamic operation of the bearing and investigates how breakdown channel parameters and operational conditions affect the temperature rise in the micro-region of bearing lubrication. Ultimately, the results of the electric thermal coupling simulation are validated through experimental tests. This study revealed that in an electric field environment, the load-bearing area of the outer ring experiences significantly more severe corrosion damage than the inner ring, whereas non-bearing areas remain unaffected by electrolytic corrosion. When the inner ring reaches a speed of 4500_rpm, the maximum widths of electrolytic corrosion pits for the outer and inner rings are measured at 89 um and 51 um, respectively. Additionally, the highest recorded temperatures for the breakdown channels in the outer and inner rings are 932 °C and 802 °C, respectively. Furthermore, as the inner ring speed increases, both the width of the electrolytic corrosion pits and the temperature of the breakdown channels rise. Specifically, at inner ring speeds of 2500_rpm, 3500_rpm, and 4500_rpm, the widths of the electrolytic pits in the outer ring raceway load zone were measured at 34 um, 56 um, and 89 um, respectively. The highest temperatures of the lubrication film breakdown channels were recorded as 612 °C, 788 °C, and 932 °C, respectively. This study provides a theoretical basis and data support for the protective and maintenance practices of traction motor bearings.

Keywords: traction motor; shaft current; electric corrosion; electric thermal coupling

check for updates

Academic Editor: Kai Cheng

Received: 10 July 2025
Revised: 29 July 2025
Accepted: 30 July 2025
Published: 1 August 2025

Citation: Yang, H.; Shi, Z.; Wang, X.; Zhang, J.; Zhang, R.; Wang, H. Simulation and Analysis of Electric Thermal Coupling for Corrosion Damage of Metro Traction Motor Bearings. *Machines* **2025**, *13*, 680. https://doi.org/10.3390/machines13080680

Copyright: © 2025 by the authors. Licensee MDPI, Basel, Switzerland. This article is an open access article distributed under the terms and conditions of the Creative Commons Attribution (CC BY) license (https://creativecommons.org/licenses/by/4.0/).

1. Introduction

The electrification of generator sets, electric locomotives, new energy vehicles, and other industries is progressing rapidly. AC motors are extensively utilized in rail transportation due to their favorable operational characteristics and control capabilities when

supplied with a variable-frequency power source, resulting in significant economic benefits. However, the axial voltage generated during the operation of AC motors induces high-frequency axial currents in the bearings [1], leading to galvanic corrosion on the working surfaces of the bearings. This phenomenon contributes to premature bearing failure and has increasingly become a predominant mode of failure [2,3]. The galvanic corrosion induced by shaft currents compromises the internal structure of the bearing and the lubricant film, causing localized microstructural changes on the contact surface and material loss [4,5]. Consequently, this results in a substantial reduction in bearing lifespan, significantly impacting the safety and reliability of the equipment [6,7]. Therefore, the issue of galvanic corrosion in bearings caused by shaft currents has garnered considerable attention from both the industrial community and academic scholars.

The damage mechanism of galvanic corrosion induced by high-frequency currents is crucial for analyzing this phenomenon. Busse et al. [8] analyzed the mechanism of shaft current generation, identifying high-frequency common-mode voltage and stray capacitance within the motor as the fundamental causes. They developed a shaft current analysis model and presented an analytical formula for calculating motor stray capacitance. Zika et al. [9] conducted experiments to electrically evaluate the damage to bearing raceways using DC, AC, and high-frequency pulsed currents, finding that high-frequency pulsed currents cause significant damage to bearings. Chiou et al. [10] identified three states of galvanic corrosion: active, transitional, and inactive. They concluded that electric current is the primary factor influencing the area of galvanic corrosion craters and derived a formula relating threshold voltage and oil film thickness as a criterion for the formation of galvanic corrosion. Bhattacharya [11] and Niskanen [12] found that the breakdown voltage of the bearing oil film decreases as the current frequency increases. Additionally, Wang [13] and Wang [14] identified that the increase in both the amplitude and frequency of the alternating voltage in current-carrying bearings directly contributes to the severity of electroerosion damage.

Pits resulting from electrocorrosion damage due to shaft currents can significantly impact on the contact between steel balls and raceway surfaces, ultimately leading to failures associated with bearing electrocorrosion damage. The predominant forms of electrocorrosion damage observed in current-carrying bearings are pitting and grooves, with pitting representing an early stage of damage failure instigated by shaft currents. He et al. [15] found that pitting corrosion originated from weak yet dense discharges of shaft current. The pitting surface comprised numerous small electrolytic pits, each indicating a melting effect resulting from the breakdown of the oil film. Lin et al. [16] discovered that the primary area of pitting corrosion on the bearing surface was attributed to the initial stage of arc discharge. As the duration of the arc discharge increased, the pitting area gradually expanded. Liu et al. [17] and Loos et al. [7] discovered that pitting corrosion manifests at the microscopic level as deeper melted pits, often accompanied by increased concentrations of carbon and oxygen. This indicates that lubricant degradation and surface damage occur simultaneously. Bond et al. [18] observed a direct relationship between the volume of electrolytic pitting and the material's melting temperature, noting that pitting increases with higher power supply currents. He et al. [15] found that under alternating current conditions, groove damage alternates between "dark stripes" and "bright stripes". Zika et al. [9] reported that although the total cumulative energy of the low-frequency alternating current in bearings is three times that of high-frequency current pulses, 10 kHz high-frequency current pulses cause groove damage on bearings in a shorter time compared to 50 Hz low-frequency alternating current. Tischmacher et al. [19] noted that the groove pitch on the inner ring of the bearing is lower than that on the outer ring, with a groove depth of approximately 3.5 μm and a width of approximately 1.3 mm. Furtmann et al. [20] found that the width of the grooves primarily depends on load, speed, roller diameter, and

bearing dynamics, while the unit area energy at the open tip of the groove on the raceway surface is influenced by material properties and contact stress levels.

Current research on electrical corrosion damage to traction motor bearings primarily focuses on the mechanisms of shaft current generation, the characteristics of electrical corrosion damage, and the influencing factors. Most studies rely on ball-and-disk testers for component-level exploratory investigations. However, there is a relative scarcity of research findings regarding the quantitative assessment of electrical corrosion damage severity in current-carrying bearings, and analyses of breakdown discharge processes have typically been conducted in a static manner. To more accurately simulate the actual operating conditions of traction motor bearings and quantitatively assess the extent of electrical corrosion damage in current-carrying bearings, a simulation analysis method that considers the dynamic processes of bearings has been proposed. This method integrates simulation-derived temperature data with the dimensions of electrical corrosion pits to evaluate electrical corrosion damage, utilizing specific lubricant film breakdown channel temperatures and electrical corrosion pit dimensions to reflect the extent of electrical corrosion damage.

This paper constructs an equivalent circuit for traction motor bearings, establishes a dynamic model for the breakdown discharge of the oil film in bearings, and conducts a detailed analysis of the oil film breakdown process. It reveals the temperature rise caused by the discharge breakdown of the oil film in current-carrying bearings under varying voltages and frequencies. Finally, it analyzes the influence of operating conditions of traction motor bearings and breakdown channel parameters on the temperature rise in the lubrication microzone and verifies the results through experimental methods. This research not only enriches the fundamental theoretical understanding of the mechanisms underlying electrical corrosion in current-carrying bearings but also provides theoretical support and engineering guidance for suppressing electrical corrosion and extending the lifespan of bearings.

2. Materials and Methods

Traction motor bearings are primarily driven by DC-AC inverter drive systems, which can lead to one significant drawback: galvanic corrosion of the bearings [21]. Statistically, the predominant failure mode of traction motor bearings is the spalling of rings or balls resulting from galvanic corrosion. Consequently, an equivalent circuit analysis of the carrier bearing is conducted to tackle the issue of galvanic corrosion-induced failure in traction motor bearings. Due to the extremely short discharge breakdown time of the lubricant film in traction motor bearings and the limited breakdown range, this paper simplifies the bearing model and focuses on the cumulative damage mechanism associated with lubricant film breakdown discharge to conduct a dynamic analysis. The dynamic characteristics of the breakdown channel discharge are characterized by calculating the time required for a steel ball to traverse the potential discharge breakdown region. Additionally, a current-carrying bearing electric thermal coupling temperature field analysis model is developed.

2.1. Current-Carrying Bearing Equivalent Circuit Construction

The microelectric spark erosion (EDM) resulting from the breakdown of the lubricating oil film in current-carrying bearings is the fundamental reason for the melting of materials on the bearing raceway and the surface of the rolling elements, resulting in the formation of pit defects. In the operational process of traction motor bearings, the insulating coating resistance and capacitance of the bearing itself, along with the resistance of the inner ring, outer ring, and steel balls, as well as the resistance and capacitance of the oil film, collectively form a mixed circuit. Since the non-carrying area of the steel ball and the raceway is

significantly larger than the bearing area, the capacitance can be disregarded [13]. Thus, the equivalent circuit of the bearing can be constructed by considering only the bearing area.

For multiple steel ball current-carrying bearings, the local schematic diagram of the equivalent capacitance is illustrated in Figure 1. The cage's main function is to evenly separate the rolling elements and prevent contact between adjacent ones. This is not displayed in Figure 1, for simplicity. The capacitance and reactance associated with the steel balls, along with the inner and outer raceways, are configured in a series arrangement, whereas the various steel balls are linked in parallel. Consequently, the equivalent capacitance and reactance of the bearing are first connected in series and then combined in parallel as a whole. When ceramic coats the bearing, the capacitance of the section with the ceramic coating is linked in series with the bearing's equivalent capacitance.

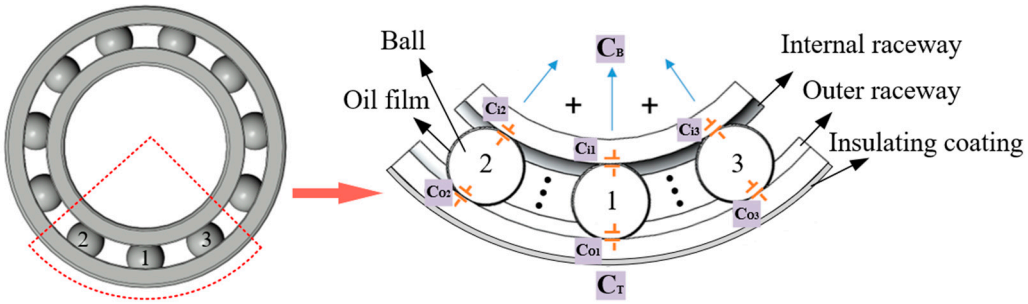


Figure 1. Models of insulated current-carrying bearings (without cage).

When the bearing area contains n grains of steel balls, the capacitance of an individual grain, represented by its inner and outer oil film, can be modeled in series. This circuit model can then be equated to n grains of steel ball unit oil films arranged in parallel, as illustrated in Figure 2. This circuit model can then be equated to n grains of steel ball unit oil films arranged in parallel, as illustrated in Figure 2. In Figure 2, R_i and R_O denote the resistances of the inner and outer rings, respectively, while R_1, R_2, and R_n indicate the resistances of the first, second, and nth steel balls. Additionally, C_T and R_T represent the capacitance and resistance of the ceramic-coated section of the outer ring, respectively. Furthermore, C_{i1} and R_{i1} represent the capacitance and resistance of the lubricating oil film between the first steel ball and the inner ring, while C_{o1} and R_{o1} denote the capacitance and resistance of the lubricating oil film between the first steel ball and the outer ring. Similarly, C_{i2} and R_{i2} represent the capacitance and resistance of the lubricating oil film between the second steel ball and the inner ring, with C_{o2} and R_{o2} indicating the capacitance and resistance of the lubricating oil film between the second steel ball and the outer ring. Finally, C_{in} and R_{in} represent the capacitance and resistance of the lubricating oil film between the nth steel ball and the inner ring, while C_{on} and R_{on} denote the capacitance and resistance of the lubricating oil film between the nth steel ball and the outer ring. From the perspective of circuit equivalence, when the bearing lubricant film is not pierced, the inner and outer raceways, steel balls, and lubricant film collectively form the equivalent capacitance of the bearing. However, when the bearing lubricant film is pierced, the steel balls come into direct contact with the raceways, resulting in a resistive state for the bearing.

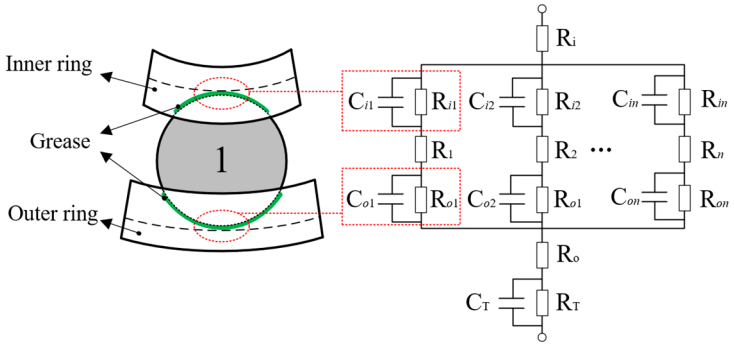


Figure 2. Equivalent circuit diagram of current-carrying bearing.

2.2. Calculation of Current-Carrying Bearing's Shaft Current

To evaluate the bearing galvanic corrosion damage through simulation analysis of the equivalent model of the traction motor bearing, it is essential to accurately calculate the current flowing through the bearing. In this study, the oil film capacitance value is determined using theoretical calculations. The oil film capacitance in the bearing's load area can be classified into two components: Hertz contact capacitance and non-Hertz contact capacitance [14]. When a load is applied to the bearing, contact occurs between the steel ball and the raceway, leading to elastic deformation that shifts from a point contact to a surface contact, which eventually creates an elliptical Hertz contact area. This capacitance can be modeled as a flat plate capacitance, which consists of two elliptical flat plate electrodes separated by a lubricant film medium.

This is represented as the Hertz contact capacitance, illustrated in the yellow grid area in Figure 3. In Figure 3, r denotes the radius of the steel ball, r_e represents the radius of the outer raceway, h_c indicates the center of the oil film thickness, and r' represents the horizontal distance projected onto the surface of the raceway at the point where the gap thickness between the ball and the raceway measures $100h_c$.

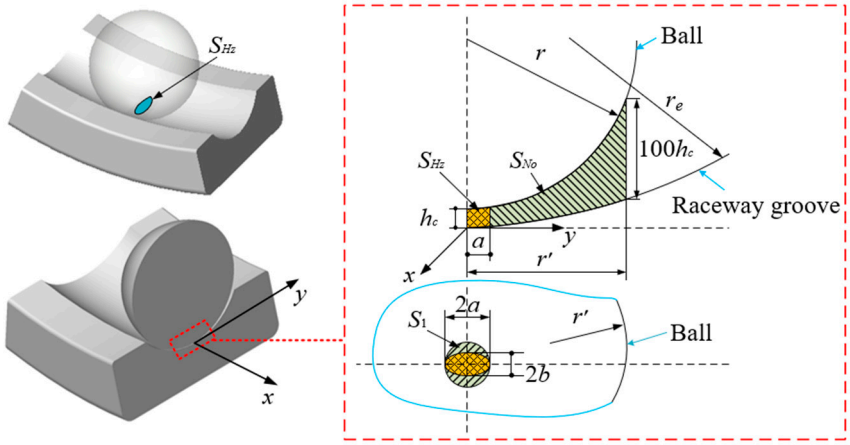


Figure 3. Effective capacitance region of the current-carrying bearing's oil film.

According to the method of calculating the capacitance between parallel polar plates [14], the Hertz contact capacitance between the steel ball and the raceway is expressed as follows:

$$C_{Hz} = \frac{\varepsilon_0 \times \varepsilon_r \times S_{Hz}}{h_c} \tag{1}$$

In the formula, ε_0 is the vacuum dielectric constant, ε_r is the relative dielectric constant, S_{Hz} is the Hertz contact area, and h_c is the center of the oil film thickness.

Non-Hertz contact capacitance is characterized as a spherical capacitance formed by steel balls, an oil film in the non-Hertz contact area, and a raceway within a specific region. The plane projection of this configuration is illustrated in Figure 3, highlighted in the green profile area. As observed in the literature [14], the bearing radial is defined for the x-axis while the axial is designated for the y-axis. In the context of bearing radial and axial calculations, the influence of r' outside the region can be neglected. The calculated deviation of the capacitance value can be maintained at less than 10%. Therefore, it is sufficient to compute the capacitance value of r'. The non-Hertz contact area capacitance consists of two components. The first component arises from the capacitance C_{S1} generated in the region S_1, which is defined by the long half-axis a of the Hertz contact ellipse minus the area corresponding to the short half-axis b of the ellipse, the other part being from the axial and radial away from the contact point within the part of the capacitance C_{No} [14]. The formulas for calculating these two capacitance components are as follows:

$$C_{S1} = 4\varepsilon_0\varepsilon_r \frac{\pi a^2 - \pi ab}{h_c} \tag{2}$$

$$C_{No} = 4\varepsilon_0\varepsilon_r \int_a^{r'} \frac{\pi r^2 \frac{l}{r} \frac{l}{\sqrt{l - \arcsin(\frac{l}{r})^2}}}{h_c + \frac{99h_c l}{r' - a}} dl \tag{3}$$

In the formula, l is the gap between the steel ball and the outer ring.

Capacitance C_{S1} and capacitance C_{No} in parallel represent the non-Hertz contact capacitance generated by the oil film between a single steel ball and the inner and outer raceways, and the non-Hertz contact equivalent capacitance of the single steel ball [14] can be expressed as follows:

$$C_{NoHz} = C_{S1} + C_{No} \tag{4}$$

For both the inner and outer raceways of the bearing, there exist C_{Hz} and C_{NoHz}, and the parallel connection of the two parts of capacitance is the total capacitance of a single steel ball with the inner and outer raceways. The total capacitance of the nth steel ball with respect to the inner and outer raceways [13] is expressed as follows:

$$C_{in(on)} = C_{Hz} + C_{NoHz} \tag{5}$$

When there are n steel balls in the load area, the equivalent capacitance of the bearing [13] can be calculated as follows:

$$C_B = C_{B1} + C_{B2} + \ldots + C_{Bn} \ldots = \frac{C_{i1}C_{o1}}{C_{i1} + C_{o1}} + \frac{C_{i2}C_{o2}}{C_{i2} + C_{o2}} + \ldots + \frac{C_{in}C_{on}}{C_{in} + C_{on}} \tag{6}$$

When an insulating coating is applied to the outer ring of the bearing, the total capacitance of the bearing consists in the insulating coating capacitance C_T in series with the lubricating oil film capacitance. The insulating coating capacitance C_T can typically be measured accurately using appropriate instruments, allowing the total capacitance of the bearing [13] to be calculated using the following formula:

$$C_{Total} = \frac{C_B C_T}{C_B + C_T} \tag{7}$$

Therefore, the formula for calculating the shaft current through the bearing [22] can be expressed as follows:

$$I = C_{Total} \frac{dU}{dt} \tag{8}$$

2.3. Oil Film Breakdown Discharge Dynamic Cumulative Damage Mechanism

Under optimal lubrication conditions, a thin and reliable lubricant film forms between the steel ball and the inner and outer ring raceways of the bearings. When common-mode voltage is applied to a bearing, an electric field is generated between the raceway and the steel balls. Should the voltage surpass the breakdown voltage limit of the oil film, a discharge phenomenon occurs between the raceway and the steel balls. The transient high temperature produced by the discharge current can rapidly reach the melting point of the bearing material, leading to the melting of the surface material of both the steel ball and the raceway, resulting in crater-like defects and the formation of welding beads on the metal subsurface. According to the theory of metal–electrolyte corrosion (MEC), the galvanic corrosion damage of bearings is a consequence of the cumulative evolution of the MEC erosion of metal materials during the breakdown of the lubricant film.

The electric breakdown process of the lubricating oil film of the current-carrying bearing is shown in Figure 4. The dynamic process of single discharge breakdown in bearing oil film can be categorized into four primary stages. First, under the action of a shaft voltage, an electric field rapidly forms between the two electrodes. As the voltage between the electrodes increases, the strength of the electric field correspondingly intensifies. Second, when the electric field strength reaches a critical threshold, the medium undergoes breakdown, resulting in a significant reduction in the resistance of the discharge gap. Consequently, the voltage across the gap decreases swiftly, and the current escalates rapidly from zero to its peak value. Third, in the presence of an electric field, electrons are accelerated and acquire energy, leading to collision ionization of high-energy ions. This process generates a high-energy ion beam that bombards the surface of the electrode plate, causing a transient state of high temperature and high pressure, converting electrical energy into kinetic energy. Finally, this kinetic energy is transformed into thermal energy through collisions. In the channel, the positive and negative pole surfaces form a transient heat source, reaching a high-temperature state that ionizes the medium between the pole plates and triggers an avalanche of electrons. As the threshold voltage of the lubricant film decreases, the film is compromised, ultimately resulting in the formation of a relatively stable breakdown channel at the point of minimal lubricant film thickness. This process leads to localized microstructural changes on the surface and material loss, thereby causing galvanic corrosion in bearings.

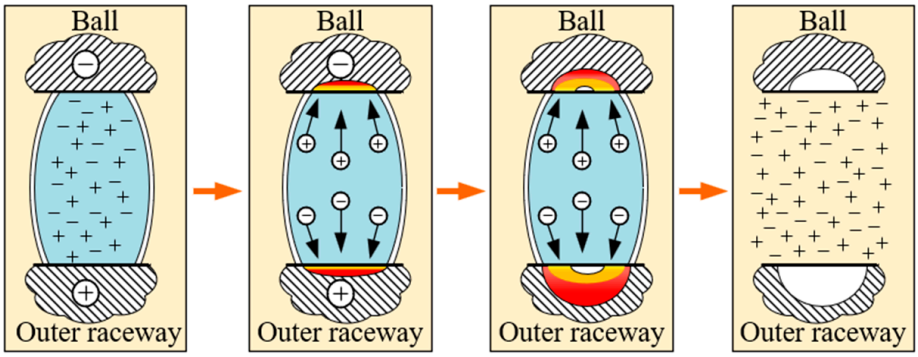


Figure 4. Schematic diagram of equivalent capacitance breakdown process of lubricating oil film in current-carrying bearings.

Although the cross-sectional area of the breakdown path at a single point in the lubricant film is very small, the high temperature and pressure from the explosion of lubricant bubbles create a larger melted volcanic crater, as depicted in Figure 5, which illustrates the galvanic corrosion damage on the traction motor bearing groove surface. Furthermore, the transient high temperature generated by the breakdown of the lubricant film reduces the surface hardness of the steel ball and the contact area of the channel, increases the roughness of the contact surface, accelerates the oxidative decomposition of the grease, and triggers thermal cracking, spalling, whitish etching cracks, and other types of damage.

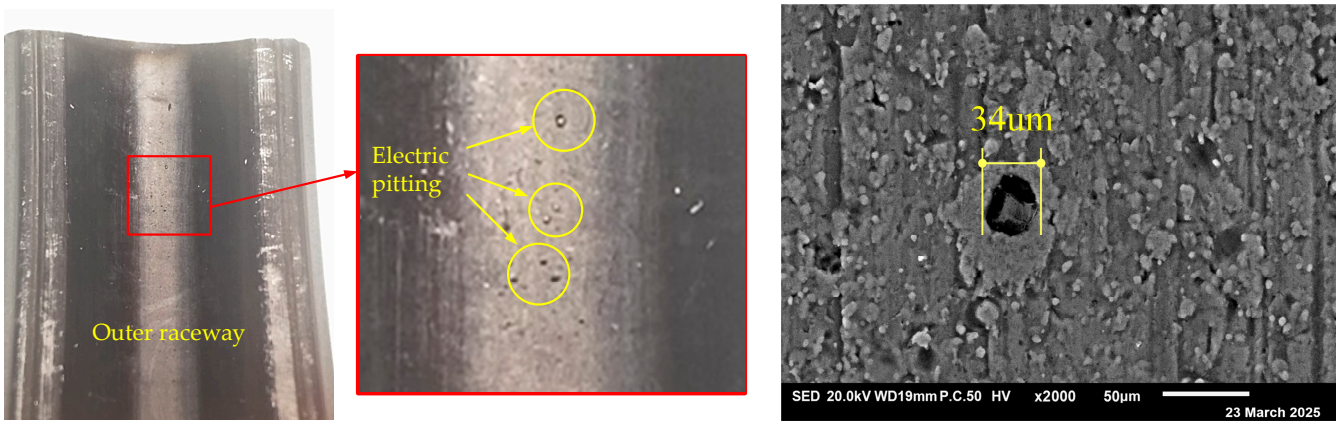


Figure 5. Electric corrosion damage on the surface of the traction motor bearing raceway: (**a**) partial enlarged view of failed sample; (**b**) electric pitting.

In the operation of metro traction motor bearings, the outer ring is fixed in place while the steel balls and the inner ring rotate. This results in dynamic contact between the steel balls and both the inner and outer raceways. Consequently, the duration of the temperature rise in individual breakdown channels is determined by the relative velocity in the contact zone. Given that the diameter of a single breakdown channel is relatively small compared to the Hertz contact surface, it can be treated as a point. The position of the Hertz contact zone continuously changes as the steel ball rolls, and the potential discharge zone formed by the individual breakdown channels of the lubricant film is illustrated in Figure 6. Since the contact between the steel ball and the raceway at any position is dynamic, the discharge breakdown of the lubricant film is also a dynamic process. Assuming that a breakdown channel is located at the center of the Hertz contact zone P, we can set a reference Hertz contact ellipse, represented by the blue area in Figure 6b. When point P is at "Position 1", which corresponds to the beginning of the reference Hertz contact area, the breakdown channel initiates discharge. As the ball rolls, point P gradually traverses the reference Hertz contact area, and the breakdown channel continues to discharge. When point P reaches "Position 2", indicating it is starting to exit the reference Hertz contact area, the breakdown channel ceases discharging. The dynamic process from "Position 1" to "Position 2" can be quantified as the time required for the steel ball to traverse the short axis of the Hertz contact ellipse, denoted as $2b$, as shown in Figure 6b.

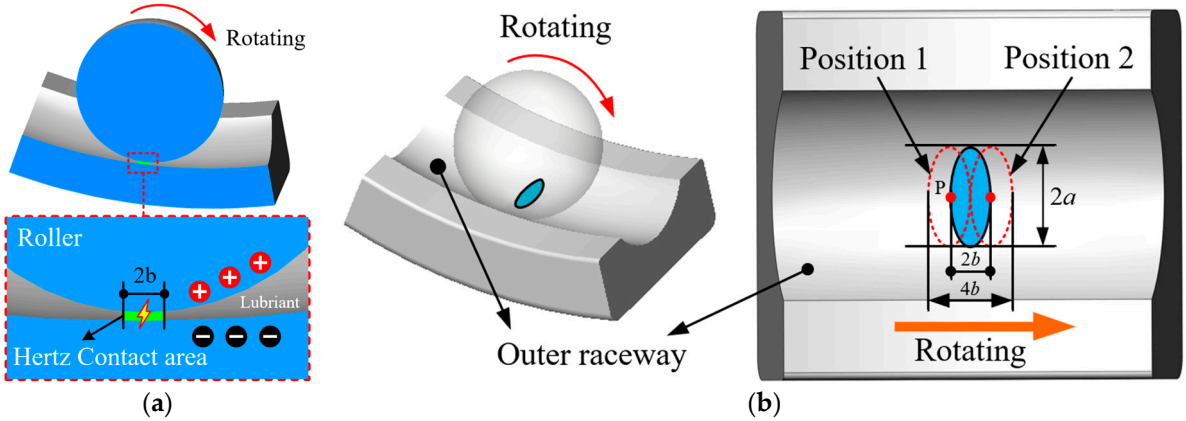


Figure 6. Schematic diagram of potential discharge area for lubricant film breakdown: (**a**) schematic diagram of axial section; (**b**) radial schematic.

Based on pure rolling theory, the time required for a ball to traverse the potential discharge breakdown region, without considering ball slippage, can be determined by using the equation provided below:

$$t = \frac{2b}{\Delta V} \tag{9}$$

In the formula, b is the short half axis of the Hertz contact ellipse; ΔV is the relative velocity of the steel ball with respect to the raceway contact area, which can be obtained from [23].

2.4. Electric Thermal Coupling Simulation Model of Traction Motor Bearing

Given the extremely small size of the etching pit between the steel ball and the raceway in the traction motor bearing, the simulation model of the bearing lubrication micro-region is reasonably simplified to ensure simulation accuracy while enhancing computational efficiency. When only radial loads are applied to the bearings, the initial simplified model is constructed using the steel ball and the inner and outer raceway units that exhibit the smallest lubricant film thickness. Further, a cylinder is intercepted with the Hertzian contact portion of the steel ball with the raceway as the center, and it is used as an electric thermal coupling simulation model of the bearing lubrication microzone. To analyze the breakdown channels of the bearing lubricant film at various locations according to the temperature change, specific breakdown points are selected for analysis. Point A is the connection between the breakdown channel and the raceway, point B is in the outer layer of the breakdown channel, located at the junction of the breakdown channel and the lubricating oil film, point C is located in the center of the breakdown channel, and point D is the connection between the breakdown channel and the rolling element. The simplified process of the electric thermal coupling model of the bearing lubrication microzone is represented in Figure 7.

In setting the size of the simulation model, it is important to consider that the Hertz contact area between the steel ball and the raceway is significantly larger than the typical dimensions of a pit caused by galvanic corrosion. Additionally, the electrical breakdown induced by the current will not encompass the entire Hertz contact area. According to observations by MUETZE [24], the width of the common galvanic corrosion crater formed when the bearing lubricating oil film is penetrated by an electric discharge measures approximately 0.4 um. Consequently, this value is designated as the cross-sectional diameter of the breakdown channel, denoted as d_A The minimum oil film thickness $h_{\min}$ between the steel ball and the raceway is taken as the length of the breakdown channel, and the other model dimensions are set in a reasonable manner. Without accounting for the random-

ness associated with the breakdown of the bearing lubricant film, the excitation current is applied at the base of the breakdown channel, with the red upward arrow in the figure indicating the direction of the current, as illustrated in Figure 7.

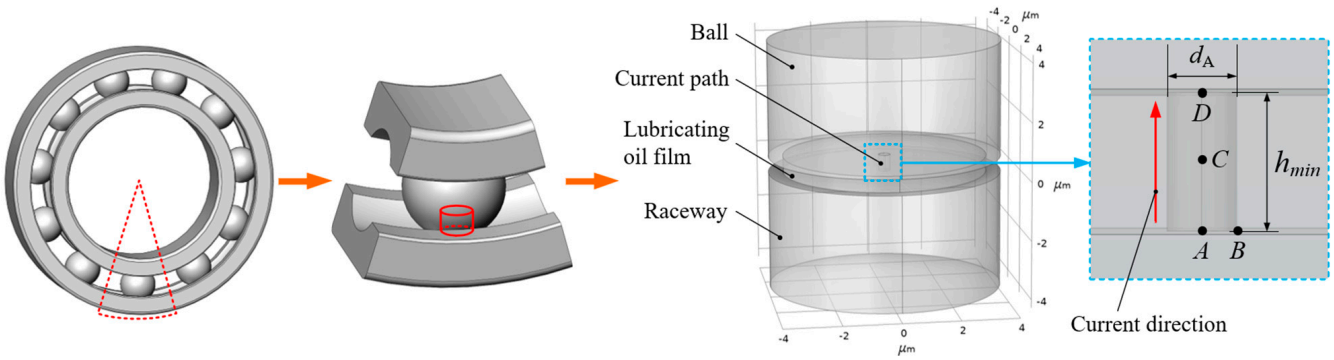


Figure 7. Simplified electric thermal coupling model of bearing.

3. Results

The breakdown of the lubricant film in bearings involves the principles of electromagnetism and thermodynamics. To tackle the interactions among these different physical fields, one can utilize the multi-physical field coupling approach. In this paper, we quantitatively analyze a micro-region simulation model of bearing lubrication using COMSOL Multiphysics 6.0 software. This analysis incorporates the current physical field and transient temperature field to simulate the temperature rise of the bearing due to high-frequency shaft current. Our goal is to further elucidate the mechanism of galvanic corrosion damage in bearings.

3.1. Shaft Current Calculation Results

In this study, we analyze 6214 M bearings with an insulating coating located at the non-driving end of a traction motor. The parameters of the bearings are detailed in Table 1, while the grease parameters are presented in Table 2.

Table 1. The 6214 M bearing parameters.

Parameter	Value	Parameter	Value
Internal diameter d/mm	70	External diameter D/mm	125
Width B/mm	24	Pitch diameter d_m/mm	97.5
Coefficient of curvature radius of inner raceway groove f_i	0.515	Coefficient of curvature radius of outer raceway groove f_e	0.525
Ball diameter D_W/mm	15.875	Number of balls N	11
Elastic modulus of steel E_0/Pa	2.08×10^{11}	Vacuum dielectric constant $\varepsilon_0/(\mathrm{F} \times \mathrm{m}^{-1})$	8.85×10^{-12}
Viscosity coefficient $\alpha/(\mathrm{Pa}^{-1})$	2.08×10^{-8}	Dielectric constant of lubricating grease ε_r	2.5

Table 2. Grease parameters.

40 °C Base Oil Viscosity	100 °C Base Oil Viscosity	Kinematic Viscosity	Density	Dynamic Viscosity
220 $\mathrm{mm}^2 \times \mathrm{s}^{-1}$	19 $\mathrm{mm}^2 \times \mathrm{s}^{-1}$	16.15 $\mathrm{mm}^2 \times \mathrm{s}^{-1}$	880 $\mathrm{kg} \times \mathrm{m}^{-3}$	0.0142 Pa × s

The capacitance value of the insulating coating on the bearings used in the test was measured to be 1.5 nF. The typical speed of the traction motor is approximately 4500_rpm. Additionally, the capacitance between the steel balls in the motor bearings and the lubricating oil film present on both the inner and outer rings is influenced by the area of Hertz contact as well as the thickness of the oil film. Consequently, this study establishes a bearing inner ring speed of 4500_rpm and a radial load of 2.5 kN. Metro traction motors are usually powered by converters and PWM inverter switches to facilitate current conversion and motor speed regulation, which often places the motor bearings under high-frequency and high-voltage conditions. To simulate the actual working conditions of the traction motor bearings, the ambient temperature is set to 25 °C. The results of the shaft current after the breakdown of the lubricant film are calculated, as shown in Table 3, using sinusoidal AC signals with an applied peak-to-peak voltage of 60 V and 90 V and voltage frequencies of 100 kHz and 120 kHz as examples.

Table 3. Shaft current at bearing oil film breakdown.

Voltage/V	Frequency/kHz	Axial Current/mA
60	100	28.26
60	120	33.93
90	100	42.41
90	120	50.89

3.2. Electric Thermal Coupling Simulation Results and Analysis

Based on the electric thermal coupling temperature field simulation model established in Section 2.4, the relevant parameters calculated are illustrated in Figure 8. Specifically, the lengths of the inner and outer ring channels correspond to the minimum oil film thickness formed between the steel ball and the inner and outer rings, respectively. The electric thermal coupling temperature field simulation was conducted using the electromagnetic heat module of COMSOL software, with the material properties of the simulation model detailed in Table 4.

Name	Expression	Value	Describe
I_con	0.449e-6[m]	4.49×10^{-7} m	Inner circle path length
O_con	0.523e-6[m]	5.23×10^{-7} m	Outer circle path length
R_con	0.2e-6[m]	2×10^{-7} m	Path radius
Maximum	0.02826[A]	0.02826 A	Maximum current value
Fre	100,000[Hz]	1×10^{5} Hz	Current frequency

Figure 8. Parameter settings for the simulation.

Table 4. Material property parameters of the simulation model.

Parameter	Ball and Raceway	Oil Film	Breakdown Pathway
Conductivity $\sigma/[\mathrm{S}\times\mathrm{m}^{-1}]$	4×10^{6}	1×10^{-11}	1×10^{-11}
Density $\rho/[\mathrm{kg}\times\mathrm{m}^{-3}]$	7850	880	880
Specific heat capacity $c/[\mathrm{J}\times(\mathrm{kg}\times\mathrm{K})^{-1}]$	475	1865	1865
Thermal conductivity $\lambda/[\mathrm{W}\times(\mathrm{m}\times\mathrm{K})^{-1}]$	44.5	0.145	0.145

The shaft current excitation is typically represented as a single high-frequency pulse characterized by a very short duration. To accurately simulate the shaft current under real operating conditions, when conducting electric thermal coupling simulation on the breakdown path of bearing lubricating oil film, apply half a cycle of sinusoidal alternating current (blue curve) and add it in the form of a single shockwave (red curve). This shockwave has a peak current of 28.26 mA and a frequency of 100 kHz. The schematic representation of the excitation current is shown in Figure 9.

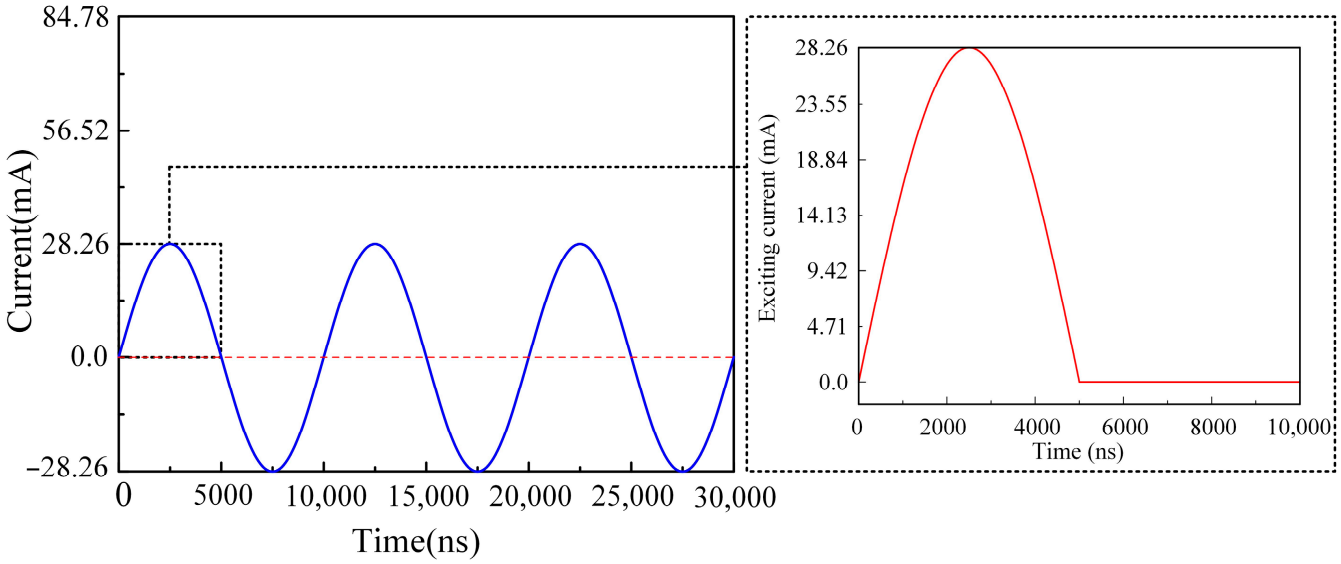


Figure 9. Schematic diagram of excitation current.

When axial currents flow through the lubricated micro-regions of the bearing and penetrate the lubricant film, significant Joule heating occurs, resulting in a change in the film-forming properties between the balls and raceways, as well as a deterioration of the lubricant film. The increase in temperature within the breakdown channel may actually attain the melting point of the material used for the bearings, which could lead to harm to the surfaces of both the raceway and the balls. Establishing the lubrication micro-region simulation model parameters for multiphysics field coupling and calculating the transient heat produced due to current loss allows for the determination of the temperature increase in the breakdown channel at various time intervals based on the temperature field.

After the breakdown of the bearing lubricant film, the steady-state temperature distribution of the inner and outer breakdown channels under varying frequencies and voltages in the electric thermal coupling simulation is determined, as illustrated in Figure 10. The illustration indicates that an increase in either voltage or frequency results in a rise in the steady-state temperature of both the inner and outer breakdown channels, with the temperature at point *C*, located at the center of the channel, being the highest. In the longitudinal direction of the breakdown channel, the temperature decreases gradually as the distance from point *C* increases. Similarly, in the transverse direction, the temperature also declines with increasing distance from point *C*, resulting in the lowest temperature at the edge of the breakdown channel. These trends in temperature distribution indicate that the energy obtained is higher closer to the center point *C* of the breakdown channel, while heat dissipation at the channel's edge occurs relatively quickly.

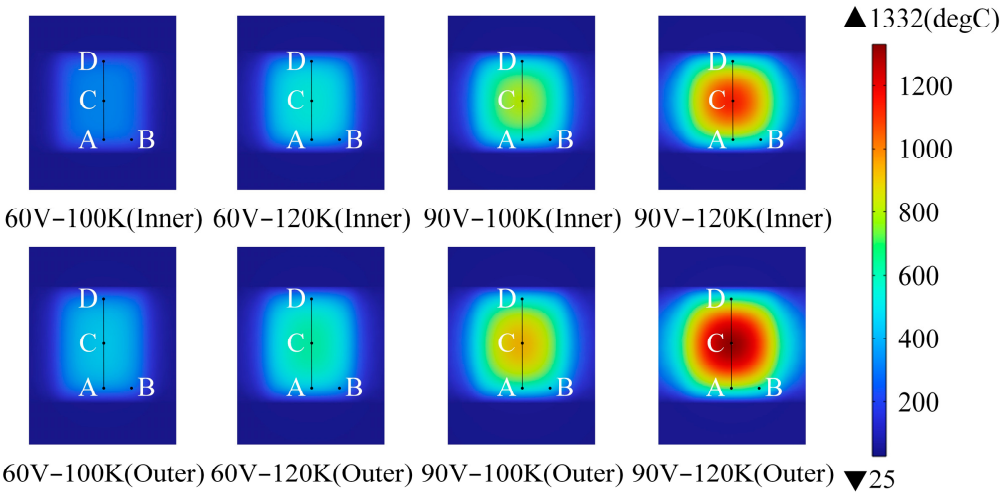


Figure 10. Steady-state temperature cloud for electric thermal coupling simulation.

The electric thermal coupling simulation was conducted under the specified working conditions, with the results of temperature variations at various positions presented in Figures 11 and 12 for different frequencies and voltages. The data indicate that the temperature at point *A*, the current excitation input point, is equivalent to that at point *D*, the symmetrical point at the opposite end of the channel. This temperature is lower than that at point *C* and higher than that at point *B*. Point *B*, located outside the current channel, exhibits the lowest temperature due to its minimal current density, which allows the generated heat to dissipate into the lubricant film surrounding the breakdown channel. The time intervals t_{1i} and t_{1o}, representing the duration of the steel ball's traversal of the potential discharge regions of the inner and outer rings, were calculated to be 1478 ns and 2208 ns, respectively. Consequently, the temperature within the breakdown channel stabilizes prior to the steel ball passing through the potential discharge region. In the subsequent figures, the times t_{1i} and t_{1o} are denoted by black and red vertical dashed lines, respectively.

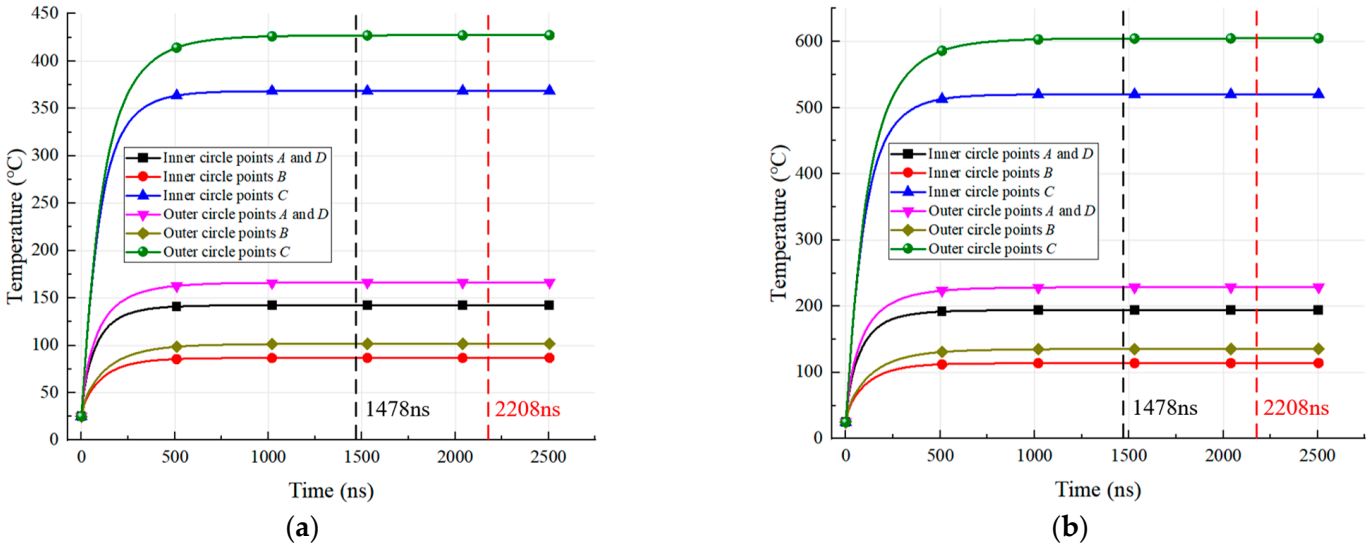


Figure 11. Temperature change curve of each point of breakdown channel at 60 V. (**a**) Temperature change curve of each point at voltage 60 V frequency 100 kHz. (**b**) Temperature change curve of each point at voltage 60 V frequency 120 kHz.

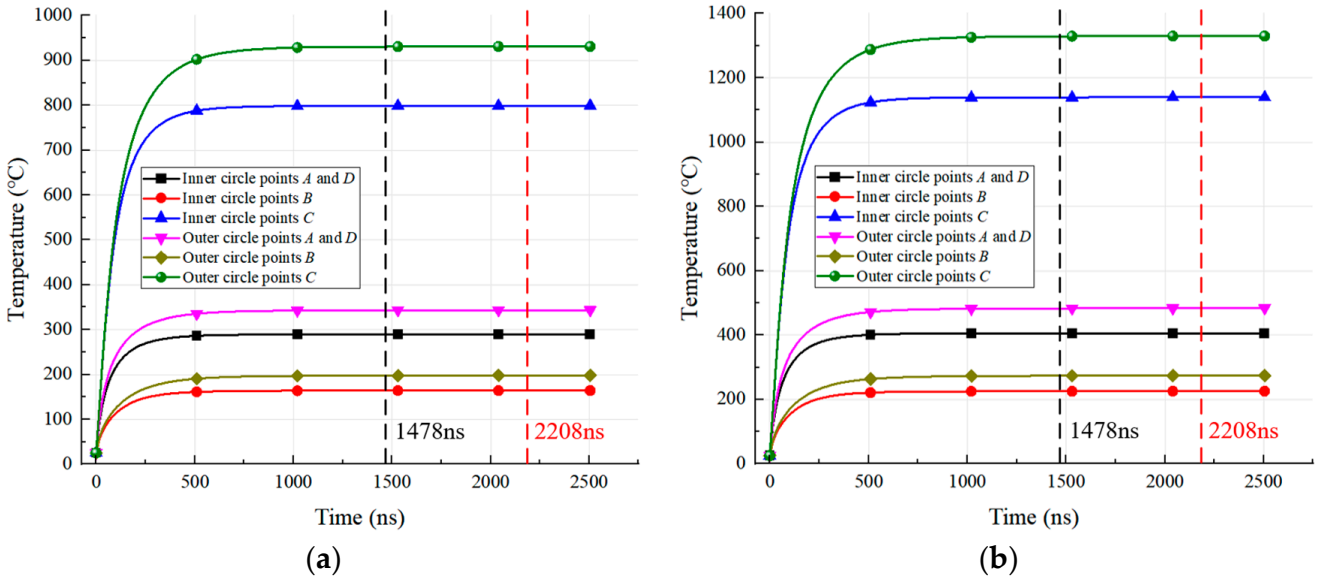


Figure 12. Temperature change curve of each point of breakdown channel at 90 V. (**a**) Temperature change curve of each point at voltage 90 V frequency 100 kHz. (**b**) Temperature change curve of each point at voltage 90 V frequency 120 kHz.

Under the applied voltage of 60 V and frequencies of 100 kHz and 120 kHz, the variation curves of channel temperature over time following the breakdown of the lubricant film are illustrated in Figure 11. The temperature in the breakdown channel increases gradually with time and stabilizes after a certain duration. For the inner raceway breakdown channel at a voltage frequency of 100 kHz, when the channel temperature rise time reaches 1478 ns, the temperature reaches 143 °C at points *A* and *D*, 88 °C at point *B*, and an alarming 370 °C at point *C*. In the case of the outer raceway breakdown channel, when the channel temperature rise time reaches 2208 ns, the temperature reaches 167 °C at points *A* and *D*, 103 °C at point *B*, and an alarming 428 °C at point *C*, as depicted in Figure 11a. For the inner raceway breakdown channel at a frequency of 120 kHz, when the channel temperature rise time reaches 1478 ns, the temperature reaches 195 °C at points *A* and *D*, 115 °C at point *B*, and an alarming 521 °C at point *C*. For the outer raceway breakdown channel, when the channel temperature rise time reaches 2208 ns, the temperature reaches 230 °C at points *A* and *D*, 137 °C at point *B*, and an alarming 606 °C at point *C*, as shown in Figure 11b.

Under the applied voltage of 90 V and at frequencies of 100 kHz and 120 kHz, the variation curves of the channel temperature over time following the breakdown of the lubricant film are presented in Figure 12. The channel temperature increases gradually with time and stabilizes after reaching a certain point. For the inner raceway breakdown channel at a frequency of 100 kHz, when the channel temperature rise time reaches 1478 ns, the temperature reaches 291 °C at points *A* and *D*, 165 °C at point *B*, and an alarming 802 °C at point *C*. In the case of the outer raceway breakdown channel, at a channel temperature rise time of 2208 ns, the temperature reaches 344 °C at points *A* and *D*, 201 °C at point *B*, and an alarming 932 °C at point *C*, as illustrated in Figure 12a. For the inner raceway breakdown channel at a frequency of 120 kHz, upon reaching a channel temperature rise time of 1478 ns, the temperature reaches 487 °C at points *A* and *D*, 227 °C at point *B*, and an alarming 1140 °C at point *C*. In the outer raceway breakdown channel, at a channel temperature rise time of 2208 ns, the temperature reaches 485 °C at points *A* and *D*, 276 °C at point *B*, and an alarming 1331 °C at point *C*, as shown in Figure 12b.

Figures 10–12 illustrate that the temperature peaks at the central point of the breakdown channel. In the longitudinal direction, the temperature decreases progressively as the distance from the point within the channel to the transverse section of the central point increases. Similarly, in the transverse direction, the temperature also diminishes gradually as the distance from the point within the channel to the longitudinal section of the central point increases, reaching its minimum at the edge of the channel.

Under identical working conditions, the thickness of the oil film on the outer ring is greater than that on the inner ring. Consequently, the temperature increase resulting from electric thermal coupling after current excitation is more pronounced in the breakdown channel of the outer ring. Furthermore, the duration for the steel ball to traverse the potential breakdown region of the outer raceway exceeds that of the inner raceway, leading to greater heat accumulation. As a result, the temperature rise is more significant, making the outer raceway of the bearing more vulnerable to galvanic corrosion damage following electric thermal coupling.

3.3. Influence of Parameters on the Temperature Rise of Bearing Lubrication Microzone Breakdown

The results of the electric thermal coupling simulation and analysis, grounded in the lubrication microzone model, indicate that applying a larger axial current to the model significantly amplifies the temperature rise within the breakdown channel. Consequently, galvanic corrosion damage is more likely to occur as the steel ball traverses the outer raceway. Therefore, this section emphasizes the investigation of the parameters associated with the outer raceway breakdown channel and examines how the working condition parameters influence the temperature rise of the bearing.

3.3.1. Influence of Breakdown Channel Length on the Temperature Rise of Bearing Lubrication Microzone Breakdown

The bearings were subjected to a rotational speed of 4500_rpm under a radial load of 2.5 kN, while a sinusoidal AC signal with a peak-to-peak voltage of 90 V and a frequency of 100 kHz was applied. By varying the length of the breakdown channel for the electric thermal coupling simulation, the impact of the breakdown channel length on the steady-state temperature at each point can be determined, as illustrated in Figure 13. The figure demonstrates that the length of the breakdown channel significantly influences the temperature rise of the bearing. As the length of the breakdown channel increases, the steady-state temperature at each point rises progressively. This phenomenon can be attributed to the single discharge breakdown of the lubricant film; with an increase in the breakdown channel length, the duration of electron bombardment on the surface of the two electrode plates is prolonged, resulting in a higher rate of electron bombardment. Consequently, this leads to greater energy release and therefore increased heat generation. Thus, the steady-state temperature at each point gradually escalates with the lengthening of the breakdown channel.

The temperature at point *C*, located at the center of the breakdown channel, exhibits a greater temperature differential compared to points *A* and *D*, which are situated at the ends of the channel, as well as point *B*, positioned at the edge of the breakdown channel. This observation suggests that, under the influence of alternating current, heat is continuously concentrated towards the center of the channel from both ends, resulting in the highest temperature at point *C*. Furthermore, the heat dissipation rate at the center of the breakdown channel is comparatively slower than that at the channel edges (points *A*, *D*, and *B*). Consequently, the steady-state temperature increase at point *C* is the most significant with an increase in the length of the breakdown channel, followed by points *A* and *D*, while the temperature change at point *B* remains relatively moderate.

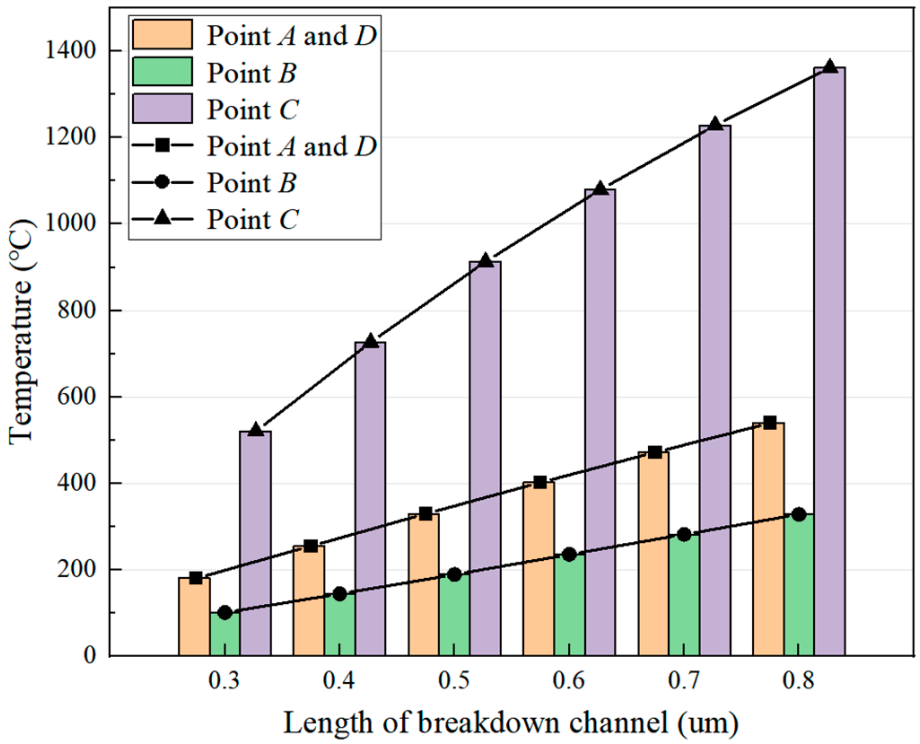


Figure 13. Effect of breakdown channel length on the steady-state temperature at each point of the breakdown channel.

3.3.2. Effect of Inner Ring Rotational Speed on the Breakdown Temperature Rise of the Bearing Lubrication Microzone

The bearings were subjected to a radial load of 2.5 kN, accompanied by a sinusoidal alternating current (AC) signal characterized by a peak-to-peak voltage of 90 V and a frequency of 100 kHz. The electric thermal coupling simulation was conducted by varying the rotational speed of the inner ring of the bearing. The resulting plots, which illustrate the time taken for the steel ball to traverse the discharge zone against the time required for the breakdown channel temperature to reach a steady state at different rotational speeds, are presented in Figure 14a. The figure indicates that the time for the inner ring of the bearing to achieve the steady state of the breakdown channel temperature is consistently less than the time required for the steel ball to pass through the discharge zone across various rotational speeds. Consequently, the rise in breakdown temperature at different speeds can be directly described by the steady-state temperature of the bearing lubrication microzone breakdown. The changes in steady-state temperature at each point of the breakdown channel at varying rotational speeds are depicted in Figure 14b. It is evident from the figure that the rotational speed of the inner ring significantly influences the steady-state temperature of the bearing lubrication microzone. As the inner ring speed increases, the temperature at each point of the breakdown channel gradually rises. Notably, the temperature at the center of the breakdown channel (point *C*) exhibits a larger temperature differential compared to the two ends of the channel (points *A* and *D*) and the edge of the breakdown channel (point *B*). With increasing rotational speed, the steady-state temperature at point *C* demonstrates a more substantial magnitude of change, followed by points *A* and *D*, while the temperature change at point *B* remains relatively smooth.

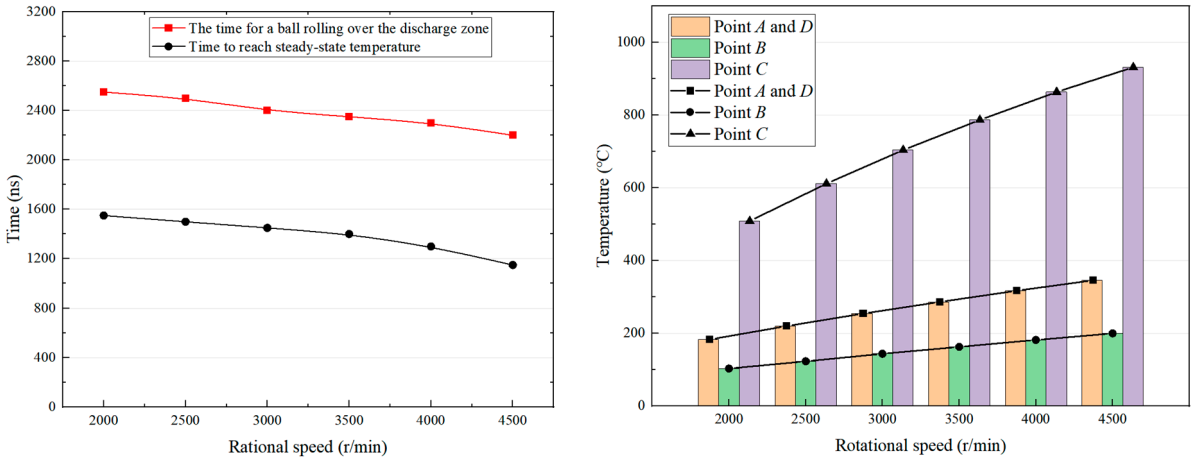


Figure 14. Effect of inner ring rotational speed on the temperature at each point of the breakdown channel. (**a**) Comparison of time *t* at different rotational speeds. (**b**) Plot of steady-state temperature change at each point of breakdown channel at different speeds.

3.3.3. Effect of Excitation Current Pulse on the Temperature Rise of Breakdown in the Microzone of Bearing Lubrication

The bearings were subjected to a rotational speed of 2000_rpm, accompanied by a radial load of 2.5 kN. *A* sinusoidal AC signal with a peak-to-peak voltage of 90 V and a frequency of 100 kHz was applied. Based on the analytical results presented in Section 4.2, the temperature rise of the breakdown channel reaches a steady state at approximately 1000 ns, which occurs significantly earlier than the duration of a single pulse (5000 ns). The start time of the excitation current pulse is selected as depicted in Figure 15, where the shaded area represents the temperature rise duration of the breakdown channel when the excitation current pulse begins at 0 ns.

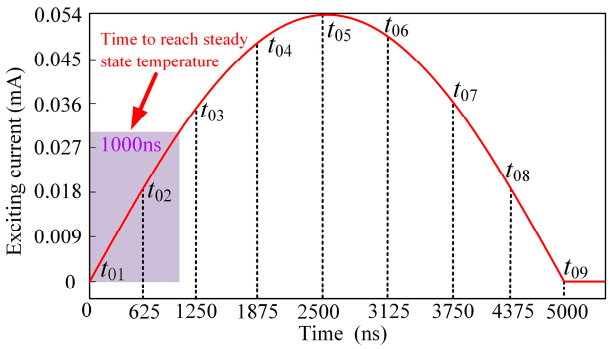


Figure 15. Selection of start time of the excitation current pulse.

By changing the excitation current pulse onset time t_{0i} for the electric thermal coupling simulation, the effect of the excitation current pulse on the steady-state temperature at each point is determined, as shown in Figure 16. The figure illustrates that as the excitation current pulse onset time increases, the steady-state temperatures at each point of the breakdown channels *A*, *B*, *C*, and *D* exhibit a trend of initially increasing and then decreasing. Notably, point *C* records the highest steady-state temperature, followed by points *A* and *D*, while point *B* maintains the lowest steady-state temperature. This variation is attributed to the differing transient excitation currents induced by the varying excitation current pulse onset times prior to the stabilization of temperature rise; these transient currents also display an initial increase followed by a decrease. Consequently, the steady-state temperature at each point in the breakdown channel reflects a similar trend. The steady-state

temperature trends correspond closely with the sinusoidal excitation current, which is essentially symmetrically distributed. When the instantaneous excitation current peaks, the steady-state temperatures at each point also reach their maximum values, with point *C* exhibiting the largest change amplitude, followed by points *A* and *D*, and point *B* showing the smallest change amplitude.

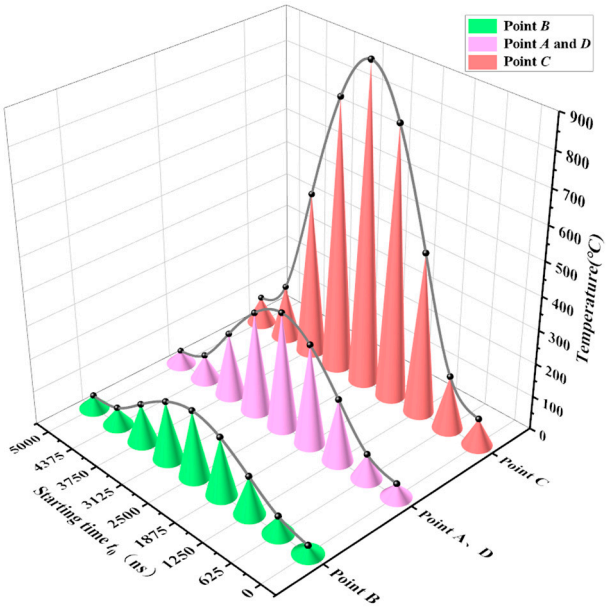


Figure 16. Effect of excitation current pulse onset time on steady-state temperature at each point.

4. Discussion

The discharge breakdown process of the bearing lubricant film occurs over a brief duration and generates significant heat, leading to transient high temperatures. Due to the challenges associated with real-time monitoring of these transient high temperatures within the micro-region of the bearing lubrication temperature field through experimental tests, this paper indirectly validates the accuracy of both the theoretical and simulation analyses by examining the damage observed on the steel balls and raceways of the bearings after operation under specified conditions.

4.1. Test Conditions

This study utilizes a self-developed traction motor bearing performance testing machine, as illustrated in Figure 17a. The testing apparatus primarily comprises a drive motor, an electric spindle, the main body of the test machine, a hydraulic loading system, a power supply system, and a data acquisition system. The machine is controlled by an industrial computer-driven system, and the drive motor employs an imported frequency conversion speed control servo motor, allowing for infinite speed regulation. The motor drives the electric spindle to rotate the inner ring of the tested bearing within the main body of the testing machine. Prior to testing, it is essential to apply a load to the test bearing via the hydraulic loading system, in accordance with the specified working conditions, and to simulate the electric field environment surrounding the test bearing using the power supply system. The testing system continuously monitors key parameters, including the number of lubricant film discharge breakdowns, voltage, temperature, and vibration changes, with the test data ultimately being collected by the data acquisition system. The working principle diagram of the testing machine is presented in Figure 17b.

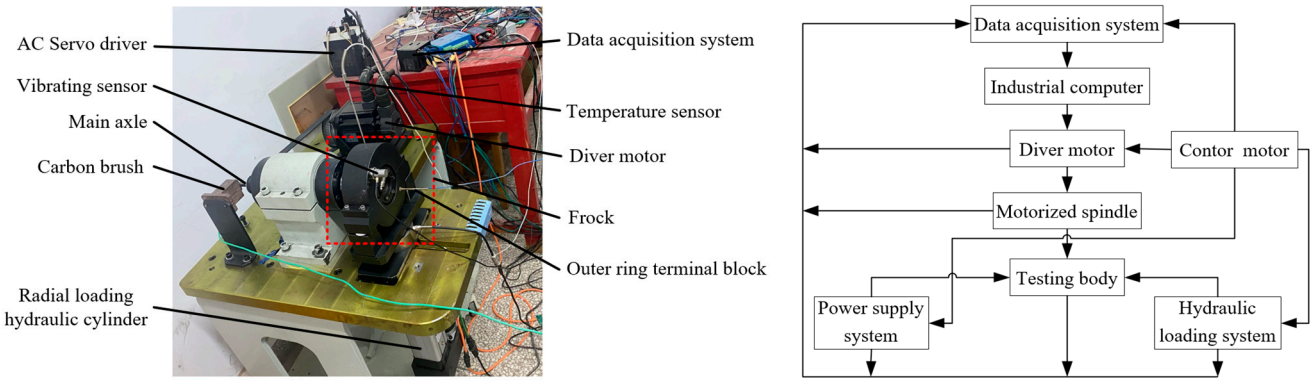


Figure 17. Current bearing testing machine and schematic diagram: (**a**) current bearing testing machine; (**b**) test machine schematic.

A power amplifier and a signal generator were employed to apply sinusoidal excitation voltage signals to the bearings. An oscilloscope was utilized to measure the variations in voltage signals among the components of the bearings. The schematic diagram of the test circuit is illustrated in Figure 18. The excitation voltage signal is output from the power amplifier connected to the signal generator and is transferred to the main spindle of the testing machine via carbon brushes. The signal then traverses the main spindle, the inner ring, the steel ball, the outer ring, the outer ring coating, and the bearing housing in sequence, ultimately connecting back to the power amplifier to form a closed-loop current loading circuit. During the measurement process, Channel 1 is designated for measuring the total voltage change in the applied signal, Channel 2 is utilized to assess the voltage change at the ends of the oil film, and Channel 3 is employed to evaluate the voltage change at the ends of the insulating coating.

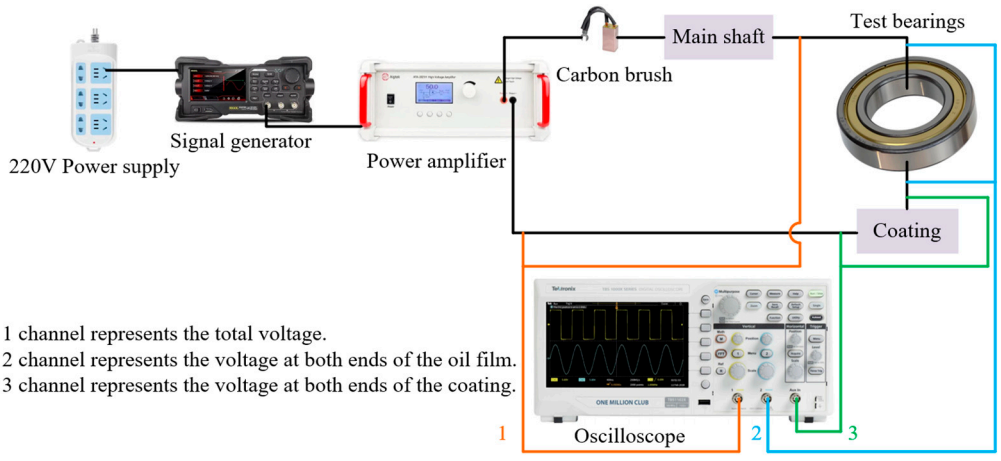
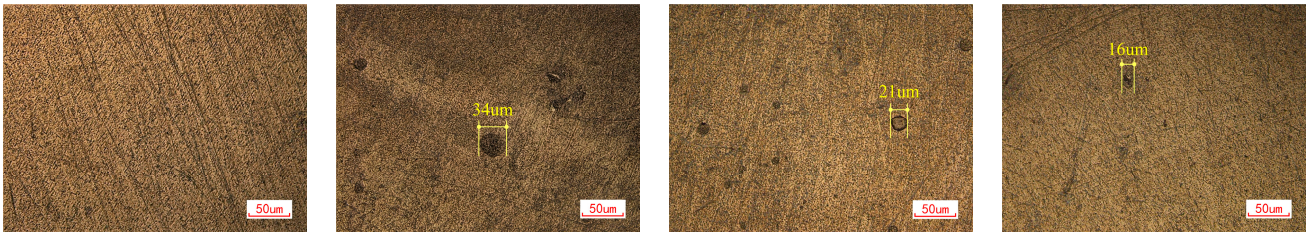


Figure 18. Experimental circuit diagram.

4.2. Comparison of Test and Simulation Results

In this experiment, three sets of 6214M bearings with insulating coatings, designated as X bearing, *Y* bearing, and *Z* bearing, were utilized. Each set of bearings was subjected to a radial load of 2.5 kN while a sinusoidal AC signal with a peak-to-peak voltage of 90 V and a frequency of 100 kHz was applied. Figures 19–22 present the cross-sectional inspection diagrams of bearings *X*, *Y*, and *Z* after 300 h of operation at speeds of 2500_rpm, 3500_rpm, and 4500_rpm, respectively, along with the corresponding actual lubricant diagrams.



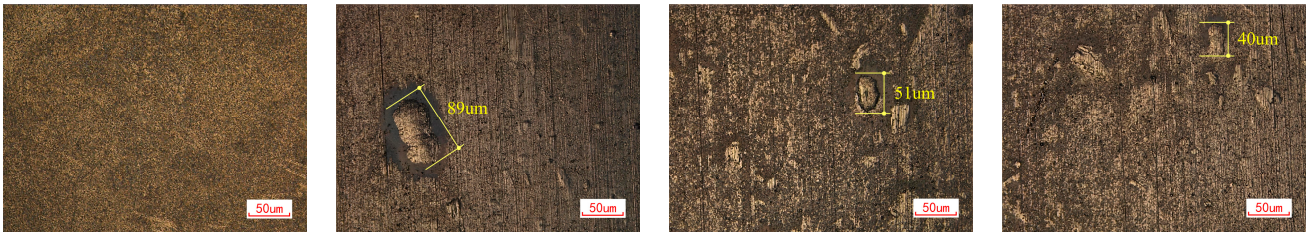
(**a**) (**b**) (**c**) (**d**)

Figure 19. Bearing slicing inspection diagram at 2500_rpm speed. (**a**) Outer raceway surface of outer ring non-load-bearing area. (**b**) Outer raceway surface in the load-bearing area of the outer ring. (**c**) Inner raceway surface. (**d**) Steel ball surface.



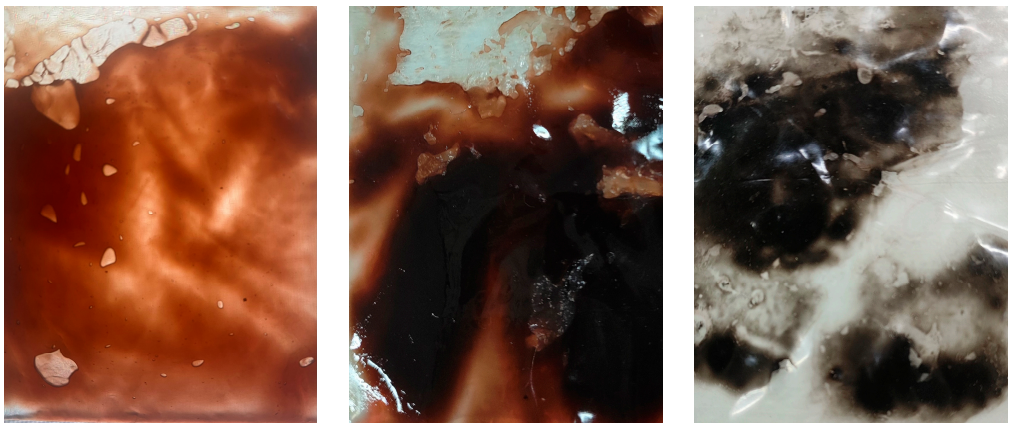
(**a**) (**b**) (**c**) (**d**)

Figure 20. Bearing slicing inspection diagram at 3500_rpm speed. (**a**) Outer raceway surface of outer ring non-load-bearing area. (**b**) Outer raceway surface in the load-bearing area of the outer ring. (**c**) Inner raceway surface. (**d**) Steel ball surface.



(**a**) (**b**) (**c**) (**d**)

Figure 21. Bearing slicing inspection diagram at 4500_rpm speed. (**a**) Outer raceway surface of outer ring non-load-bearing area. (**b**) Outer raceway surface in the load-bearing area of the outer ring. (**c**) Inner raceway surface. (**d**) Steel ball surface.



(**a**) (**b**) (**c**)

Figure 22. Lubricant grease images at different rotational speeds: (**a**) lubricant grease appearance at 2500_rpm; (**b**) lubricant grease appearance at 3500_rpm; (**c**) lubricant grease appearance at 4500_rpm.

This study conducts systematic experimental tests and electric thermal coupling simulation to thoroughly investigate the evolution patterns and influencing mechanisms of electrolytic corrosion damage in current-carrying bearings. The experimental and simulation results are compared and discussed below:

1. The test results indicate that when the inner ring speed of the bearing reaches 4500_rpm, the maximum electrolytic pit width on the outer raceway reaches 89 um, significantly greater than the 51 um observed on the inner raceway. Electrothermal coupling simulation analysis reveals that the maximum temperature at the lubricant film breakdown channel between the outer raceway and the steel balls is 932 °C, which is also higher than the 802 °C recorded on the inner raceway. Comparative analysis confirms that the outer raceway is more susceptible to severe electrocorrosion than the inner raceway. The underlying mechanisms for this phenomenon are as follows: first, the outer raceway has a longer heat dissipation path and lower thermal conductivity efficiency, making it difficult for the heat generated by electrocorrosion discharge to dissipate quickly, resulting in significant heat accumulation; second, due to the fixed load distribution, current density tends to concentrate in specific areas, forming hotspots of high current density. In contrast, the inner raceway benefits from better thermal conductivity and a more uniform current distribution, effectively reducing the risk of localized electrolytic corrosion. Therefore, maintenance strategies for bearings should prioritize the protection of the outer raceway, employing methods such as surface insulating coatings and lubricants with lower conductivity to mitigate the risks of electrolytic corrosion in this region.
2. The test results indicate that when the outer ring of the bearing is fixed and the inner ring rotates at speeds of 2500_rpm, 3500_rpm, and 4500_rpm, the width of the electrolytic corrosion pits in the outer raceway load-bearing area shows a significant increase, reaching 34 um, 56 um, and 89 um, respectively. The electrothermal coupling simulation results demonstrate that the maximum temperatures of the lubricating oil film breakdown channels under the corresponding operating conditions are 612 °C, 788 °C, and 932 °C, respectively. A comparative analysis reveals that as the inner ring speed increases, the temperature generated after the lubricating oil film breakdown significantly rises, and the width of the electrolytic pits also increases accordingly. The underlying mechanism is as follows: increased rotational speed leads to thicker lubricating oil films, prolonging the ion acceleration time during discharge and increasing the kinetic energy impacting the surface, ultimately resulting in higher temperatures and larger electrocorrosion damage. Therefore, to mitigate the severity of bearing electrocorrosion damage, it is advisable to reduce the bearing rotational speed as much as possible while ensuring compliance with operational performance requirements.
3. The test results indicate that when the outer ring of the bearing is fixed and the inner ring rotates at speeds of 2500_rpm, 3500_rpm, and 4500_rpm, the width of the electrolytic pits formed on the surface of the steel balls in the load-bearing area measures 16 um, 21 um, and 40 um, respectively, demonstrating a positive correlation with increasing rotational speed. Notably, no electrical corrosion damage was observed in the non-load-bearing area of the outer raceway. This phenomenon suggests that electrical corrosion damage occurs on the surface of the steel balls, primarily concentrated in the load-bearing area. This distribution can be attributed to the thicker oil film present in the non-load-bearing area, which results in a diminished capacitive effect, hindering effective discharge phenomena. Consequently, maintenance strategies for the bearing, such as altering the load-bearing position of the outer ring or implementing protective measures focused on the outer raceway outside the load-bearing area, can be adopted

to mitigate electrical corrosion damage to the steel balls and outer raceway, thereby extending the service life of the bearing.

4. Test results indicate that when the outer ring of the bearing is fixed and the inner ring rotates at speeds of 2500_rpm, 3500_rpm, and 4500_rpm, the color of the grease undergoes a noticeable transformation: from a reddish-brown indicating good condition, to a reddish-black signifying a mixed normal condition, and finally to a black representing an abnormal condition. This phenomenon is attributed to the increase in rotational speed, which elevates the breakdown temperature of the lubricating oil film, leading to the thermal oxidation degradation of the grease. Elevated temperatures cause the molecular chains of the base oil and thickener to decompose, resulting in the formation of carbonized products and oxides. This process leads to a darker grease color, reduced viscosity, and deteriorated lubrication performance. Based on this mechanism, to ensure reliable bearing operation, it is advisable to select grease with lower conductivity to mitigate electrolytic corrosion damage. Furthermore, regular monitoring of grease color changes should be implemented to evaluate bearing condition, facilitating timely maintenance and replacement to ensure optimal lubrication performance.

5. Conclusions

This paper analyzes the mechanism of lubricant film breakdown discharge damage in the dynamic operation of traction motor bearings. It constructs an electrically and thermally coupled simulation and analysis model of the lubricant film breakdown channel in traction motor bearings and experimentally verifies the extent of galvanic corrosion damage. Based on the research into the electric thermal coupling simulation of galvanic corrosion damage in traction motor bearings, the following conclusions are drawn:

1. The outer raceway is more susceptible to severe electrolytic corrosion than the inner raceway. Specifically, when the speed of the inner ring reaches 4500_rpm, the maximum width of electrolytic pits on the outer raceway of the bearing reaches 89 um, which is significantly larger than the 51 um observed on the inner raceway. Furthermore, the highest temperature recorded in the breakdown channel of the outer raceway was 932 °C, exceeding the 802 °C measured in the inner raceway. Therefore, it is imperative that bearing design and maintenance prioritize the protection of the outer raceway. This can be achieved by applying an insulating coating to the surface of the outer raceway or utilizing lubricants with lower conductivity to mitigate the risk of electrical corrosion in this area.
2. As the speed of the inner ring increases, the temperature generated by the breakdown of the bearing lubricating oil film rises significantly, leading to a corresponding increase in the width of the electrolytic pits. Specifically, at inner ring rotational speeds of 2500_rpm, 3500_rpm, and 4500_rpm, the widths of the electrolytic pits in the load-bearing area of the outer raceway are measured at 34 um, 56 um, and 89 um, respectively. The maximum temperatures of the lubricant film breakdown channels are recorded at 612 °C, 788 °C, and 932 °C, respectively. To extend the service life of traction motor bearings, it is recommended to reduce the bearing rotational speed while ensuring compliance with operational performance requirements.
3. No electrolytic corrosion damage was observed in the non-load-bearing area of the outer raceway; however, electrolytic corrosion did occur on the surface of the steel balls. Specifically, at inner ring speeds of 2500_rpm, 3500_rpm, and 4500_rpm, no electrolytic pits formed in the non-load-bearing area of the outer raceway. In contrast, the width of the electrolytic pits that developed on the ball surface measured 16 um, 21 um, and 40 um, respectively. To enhance the service life of traction motor bearings,

either the load-bearing position of the outer ring can be adjusted or an insulating coating may be applied to the outer raceway in the load-bearing area.

4. When the inner ring speed is 2500_rpm, 3500_rpm, and 4500_rpm, the color of the grease changes significantly: from a reddish-brown indicating good condition, to a reddish-black signifying a mixed normal condition, and finally to a black representing an abnormal condition. To ensure good lubrication of the bearing, it is advisable to select grease with low electrical conductivity or to monitor changes in grease color as a means to assess the condition of the bearing. Timely maintenance and replacement of the grease are also essential.

Author Contributions: Conceptualization, Z.S. and H.Y.; data curation, Z.S. and X.W.; formal analysis, Z.S. and H.W.; funding acquisition, H.W.; investigation, Z.S., H.Y. and H.W.; methodology, H.Y. and H.W.; project administration, X.W. and H.W.; resources, J.Z.; software, Z.S.; supervision, H.Y. and H.W.; validation, X.W. and R.Z.; writing—original draft, Z.S. and H.Y.; writing—review and editing, H.Y., X.W. and H.W. All authors have read and agreed to the published version of the manuscript.

Funding: This research was founded by the National Natural Science Foundation of China (52005158) and the Ningbo Key Research and Development Program and "Jiebang Gua-shuai" Project (2023Z006).

Data Availability Statement: The data used to support the findings of this study are available from the corresponding author upon request.

Conflicts of Interest: Author Xuelan Wang is employed by Ningbo Great Group Co., Ltd. The other authors declare that the research was conducted in the absence of any commercial or financial relationships that could be construed as a potential conflict of interest.

References

1. Luo, Z.X. Research on Traction Motor Bearing Electric Erosion of Metro Vehicle and Its Improvement Measures. *J. Electr. Drive Locomot.* **2021**, *2021*, 37–41.
2. Cai, M.Y.; Chen, X.M.; Nie, S.Y. Research on electric corrosion of generator bearings for wind turbine. *J. Ship Eng.* **2019**, *41*, 302–306+310.
3. Wang, Q.Q.; Liu, R.F.; Ren, X.J. The Motor Bearing Discharge Breakdown Based on the Multi-Physics Field Analysis. *Trans. China Electrotech. Soc.* **2020**, *35*, 4251–4257.
4. Plazenet, T.; Boileau, T.; Caironi, C.C.; Nahid-Mobarakeh, B. Influencing Parameters on Discharge Bearing Currents in Inverter-Fed Induction Motors. *IEEE Trans. Energy Convers.* **2021**, *36*, 940–949. [CrossRef]
5. Bao, J.; Xu, C.B.; Zhao, H.C. Research on Electric Corrosion Failure of Drive Motor Bearing. *J. Microtome* **2022**, *50*, 58–64.
6. Xie, G.; Luo, J.; Guo, D.; Liu, S.; Li, G. Damages on the lubricated surfaces in bearings under the influence of weak electrical currents. *Sci. China Technol. Sci.* **2013**, *56*, 2979–2987. [CrossRef]
7. Loos, J.; Bergmann, I.; Goss, M. Influence of High Electrical Currents on WEC Formation in Rolling Bearings. *Tribol. Trans.* **2021**, *64*, 708–720. [CrossRef]
8. Busse, D.F.; Erdman, J.M. The effects of PWM voltage source inverters on the mechanical performance of rolling bearing. *IEEE Trans. Ind. Appl.* **1997**, *32*, 567–576. [CrossRef]
9. Zika, T.; Gebeshuber, I.C.; Buschbeck, F.; Preisinger, G.; Gröschl, M. Surface analysis on rolling bearings after exposure to defined electric stress. *Proc. Inst. Mech. Eng. Part J J. Eng. Tribol.* **2009**, *223*, 787–797. [CrossRef]
10. Chiou, Y.-C.; Lee, R.-T.; Lin, C.-M. Formation criterion and mechanism of electrical pitting on the lubricated surface under AC electric field. *Wear* **1999**, *236*, 62–72. [CrossRef]
11. Bhattacharya, S.; Resta, L.; Divan, D.M.; Novotny, D.W.; Lipo, T.A. Experimental comparison of motor bearing currents with PWM hard and soft switched voltage-source inverters. *IEEE Trans. Power Electron.* **1996**, *14*, 552–562. [CrossRef]
12. Niskanen, V.; Muetze, A.; Ahola, J. Study on Bearing Impedance Properties at Several Hundred Kilohertz for Different Electric Machine Operating Parameters. *IEEE Trans. Ind. Appl.* **2014**, *50*, 3438–3447. [CrossRef]
13. Wang, Z.; Mao, S.; Tian, H.; Su, B.; Cui, Y. Simulation Analysis and Experimental Research on Electric Thermal Coupling of Current Bearing. *Lubricants* **2024**, *12*, 73. [CrossRef]
14. Wang, Q. Research on Capacitances Calculation and the Bearing Damage Degree in Bearing Currents of AC Motors. Master's Thesis, Beijing Jiaotong University, Beijing, China, 2021.

15. He, F.; Xie, G.; Luo, J. Electrical bearing failures in electric vehicles. *Friction* **2020**, *8*, 4–28. [CrossRef]
16. Lin, C.-M.; Chiou, Y.-C.; Lee, R.-T. Pitting mechanism on lubricated surface of Babbitt alloy/bearing steel pair under ac electric field. *Wear* **2001**, *249*, 132–141. [CrossRef]
17. Liu, W. The prevalent motor bearing premature failures due to the high frequency electric current passage. *Eng. Fail. Anal.* **2014**, *45*, 118–127. [CrossRef]
18. Bond, S.; Jackson, R.L.; Mills, G. The influence of various grease compositions and silver nanoparticle additives on electrically induced rolling-element bearing damage. *Friction* **2024**, *12*, 796–811. [CrossRef]
19. Tischmacher, H.; Gattermann, S. Multiple signature analysis for the detection of bearing currents and the assessment of the resulting bearing wear. In Proceedings of the International Symposium on Power Electronics Power Electronics, Electrical Drives, Automation and Motion, Sorrento, Italy, 20–22 June 2012; pp. 1354–1359.
20. Furtmann, A. Elektrisches Verhalten Von Maschinenelementen Im Antriebsstrang. Ph.D. Thesis, Leibniz Universität Hannover, Hannover, Germany, 2017.
21. Chi, L.Q.; Zhang, D.H.; Zhao, J.Q. Research Progress on the Mechanism and Mitigation Measure of Electrical Corrosion Damage in Rotating Motor Bearings. *J. Electrotechnol.* **2024**, *39*, 6409–6430.
22. Tang, J. *Electrotechnics*, 2nd ed.; Higher Education Press: Beijing, China, 2005; pp. 64–65.
23. Deng, S.E.; Jia, Q.Y.; Xue, J.X. *Principles of Rolling Bearing Design*, 2nd ed.; China Standard Press: Beijing, China, 2014; pp. 138–139.
24. Muetze, A.; Binder, A.; Vogel, H.; Hering, J. What can bearings bear? *IEEE Ind. Appl. Mag.* **2006**, *12*, 57–64. [CrossRef]

Disclaimer/Publisher's Note: The statements, opinions and data contained in all publications are solely those of the individual author(s) and contributor(s) and not of MDPI and/or the editor(s). MDPI and/or the editor(s) disclaim responsibility for any injury to people or property resulting from any ideas, methods, instructions or products referred to in the content.